

**Direct scattering processes and signatures of chaos in quantum waveguides**

G. B. Akguc and L. E. Reichl

*Center for Studies in Statistical Mechanics and Complex Systems, The University of Texas at Austin, Austin, Texas 78712*

(Received 17 May 2002; revised manuscript received 27 November 2002; published 8 April 2003)

The effect of direct processes on the statistical properties of deterministic scattering processes in a chaotic waveguide is examined. The single-channel Poisson kernel describes well the distribution of  $S$ -matrix eigenphases when evaluated over an energy interval. When direct processes are transformed away, the scattering processes exhibit universal random matrix behavior. The effect of chaos on scattering wave functions, eigenphases, and time delays is discussed.

DOI: 10.1103/PhysRevE.67.046202

PACS number(s): 05.45.Mt, 05.60.Gg, 73.23.Ad, 73.50.Bk

**I. INTRODUCTION**

In 1957, Wigner proposed the use of statistical measures to analyze complex nuclear scattering data [1]. It was soon found that, in some nuclear scattering data, the spacing between scattering resonances was distributed in a manner similar to the spacing of energy levels of a Gaussian random Hamiltonian [2]. In the 1960s, extensive work was done to develop a systematic theory of the statistical properties of random Hermitian matrices [3,4] and random unitary matrices [5,6]. The general criterion for constructing these random matrices is that they minimize information. In 1979, the appearance of random matrixlike behavior in quantum systems was linked to underlying chaos in the classical deterministic dynamics of these systems [7–10]. Since then a large body of work has developed linking the statistical properties of bounded and open quantum systems to underlying deterministic chaos [11–13].

Historically, there have been two different approaches to describing the statistics of quantum scattering processes in chaotic systems. One approach [14] begins directly with the Hamiltonian and uses it to build the scattering matrix. The other approach [15,16] begins directly with the scattering matrix. In both cases, random matrices are used to describe scattering processes and the statistical properties of the eigenphases of the scattering matrix and partial delay times can be obtained and compared to experiment. There has been considerable success in recent years to link the results and predictions of these two approaches [17].

The connection between the statistical properties of scattering processes and underlying chaos is not straightforward because scattering events may involve either reactive processes or direct processes. Reactive scattering processes are those for which an incident particle becomes engaged with the dynamics in the reaction region, and may be delayed there for a considerable time. Direct processes are those for which the particle passes through the reaction region without becoming significantly engaged in the reaction region. One prediction of the random matrix theory (RMT) of scattering is that, if the scattering process is truly chaotic, the average value of the  $S$  matrix will be zero. However, if direct processes are present this will not happen.

In this paper, we will study the deterministic scattering of a quantum particle in a two-dimensional ballistic waveguide which has a classically chaotic cavity formed by a ripple

billiard connected to a single lead at one end (see Fig. 1). The ripple billiard is particularly well suited to the use of the reaction matrix theory approach to scattering [18], because a simple coordinate transformation [19,20] allows us to construct a Hamiltonian matrix and thus an eigenvalue equation for the basis states inside the cavity. We will compare the results of deterministic scattering from the chaotic cavity to some recent predictions of random matrix theory as regards the scattering process. The open geometry of the waveguide in Fig. 1 ensures that direct processes will play an important role in scattering. We show that the contribution of the direct processes to the scattering can be transformed out and the statistical properties of the reactive part of the scattering process can be compared to random matrix predictions. Our discussion focuses on quantum particles and we will use parameters appropriate for electrons in waveguides made with GaAs, for which a number of experiments have been done [21–23]. However, our results also apply to electromagnetic waves in flat microwave cavities, because the eigenmodes in these cavities satisfy a Schrodinger-like equation [24–26].

We begin in Sec. II by reviewing the reaction matrix theory of deterministic scattering in the ballistic waveguide and we study some properties of the cavity basis states. In Sec. III, we study various statistical properties of the eigenphases of the waveguide scattering matrix ( $S$  matrix). We show that, when the cavity dynamics is chaotic, the deterministic  $S$ -matrix eigenphases exhibit level repulsion and their distribution is well described by a Poisson kernel. In Sec. IV, we compare the distribution of partial delay times for the deterministic scattering process to the predictions of

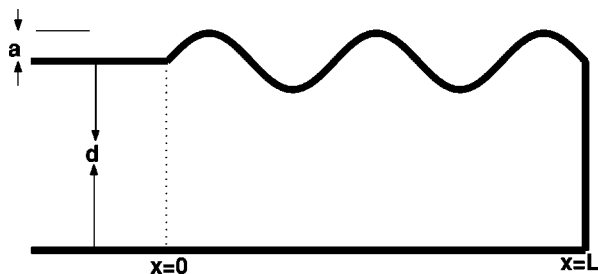


FIG. 1. The geometry of the two-dimensional ballistic waveguide used in our calculations;  $a$  is the half-width of the ripple,  $d$  is the width of the lead and the average width of the cavity. The ripple cavity extends from  $x=0$  to  $x=L$ .

random matrix theory. Finally, in Sec. V we give concluding remarks.

## II. REACTION MATRIX DESCRIPTION OF SCATTERING

We will explore the behavior of a particle of mass  $m$  in a ballistic waveguide as it scatters from the ripple cavity shown in Fig. 1. A particle with energy  $E$  enters the cavity from the left along a straight lead that has infinitely hard walls. The particle wave is reflected back to the left by an infinitely hard wall located at  $x=L$ . The dynamics inside the cavity,  $0 < x < L$ , can range from mixed to fully chaotic as the ripple amplitude is varied. The Schrödinger equation, which describes propagation of a particle wave,  $\Psi(x,y,t)$ , in the waveguide at time  $t$ , is given by

$$i\hbar \frac{\partial \Psi(x,y,t)}{\partial t} = \hat{H} \Psi(x,y,t) = \left[ -\frac{\hbar^2}{2m} \left( \frac{\partial^2}{\partial x^2} + \frac{\partial^2}{\partial y^2} \right) + V(x,y) \right] \Psi(x,y,t), \quad (2.1)$$

where  $\hat{H}$  is the total Hamiltonian of the particle in the waveguide and  $\hbar$  is the Planck's constant. The potential  $V(x,y)$  has the following properties:  $V(x,y) = \infty$  for  $(L \leq x < \infty)$ ;  $V(x,0) = \infty$  for  $(-\infty \leq x \leq L)$ ;  $V(x,y = g(x)) = \infty$  for  $(0 < x < L)$ ; and  $V(x,y = d) = \infty$  for  $(-\infty < x < 0)$ ; where  $g(x) = d + a \sin(5\pi x/L)$  gives the contour of the ripple,  $d$  is the average width of the cavity,  $L$  is the length, and  $a$  is the ripple amplitude. In all subsequent sections, we take the particle mass to be the effective mass of an electron in GaAs,  $m = 0.067m_e$ , where  $m_e$  is the free electron mass. An energy eigenstate  $|E\rangle$  with energy  $E$  satisfies the equation  $\hat{H}|E\rangle = E|E\rangle$ , and evolves as  $\Psi(x,y,t) = \langle x,y|E\rangle e^{-iEt/\hbar}$ .

As shown in Ref. [20], the waveguide energy eigenstates can be expressed in the form

$$\langle x,y|E\rangle = \sum_{j=1}^{\infty} \gamma_j \phi_j(x,y) + \sum_{n=1}^{\infty} \Gamma_n \Phi_n(x,y). \quad (2.2)$$

The states  $\Phi_n(x,y)$  are the basis states in the lead ( $x \leq 0$ ),

$$\Phi_n(x,y) \equiv \langle x,y|\Phi_n\rangle = \sqrt{\frac{2}{d}} \chi_n(x) \sin\left(\frac{n\pi y}{d}\right) \quad (2.3)$$

( $n = 1, 2, \dots, \infty$ ). These will consist of both propagating and evanescent modes, as we will discuss below. The states  $\phi_j(x,y) \equiv \langle x,y|\phi_j\rangle$  ( $j = 1, 2, \dots, \infty$ ) are the basis states in the cavity ( $0 \leq x \leq L$ ). In practice, we truncate the number of cavity basis states to some large but finite number  $M$ . The value of  $M$  is determined by the accuracy desired for the calculation. The coefficients  $\Gamma_n$  and  $\gamma_j$  in Eq. (2.2) are defined as  $\Gamma_n = \langle \Phi_n|E\rangle$  and  $\gamma_j = \langle \phi_j|E\rangle$ .

A complete set of basis states,  $\phi_j(x,y)$ , inside the ripple cavity has been obtained by solving the Schrodinger equation in the cavity, using Neumann boundary conditions  $[(d\phi_j/dx)_{x=0} = 0]$  at the entrance ( $x=0$ ), and Dirichlet

boundary conditions  $[\phi_j(x,y) = 0]$  at the walls. We obtained the eigenfunctions  $\phi_j(x,y)$  and the associated eigenvalues  $\lambda_j$  using the transformation technique discussed in Ref. [20], Sec. V.

In Fig. 2(a), we show a Poincare surface of section for a classical particle in a closed ripple cavity with the same shape as in Fig. 1, and with hard walls. We choose  $d = 101 \text{ \AA}$ ,  $L = 511 \text{ \AA}$ , and  $a = 1.0 \text{ \AA}$ . We have plotted Birkhoff coordinates  $p_x/p = \cos(\alpha)$  versus  $x$ , each time the particle hits the lower wall at point  $x$  ( $\alpha$  is the angle between the wall and the momentum). For these billiard dimensions, the classical phase space contains a mixture of regular orbits, nonlinear resonances, and chaotic motion. If we increase the ripple amplitude  $a$ , there is a range of values of  $a$  for which the classical motion appears to become totally chaotic. For the scattering system (with one end of the cavity open), periodic orbits and nonlinear resonance regions cannot be reached classically by a particle that enters from the left, but quantum mechanically tunneling into these regions is possible as we will show in Sec. IV (see also Ref. [27]). In Figs. 2(b–e), we show Husimi plots of [13] quantum Poincaré surfaces of section [28] of cavity basis states,  $\phi_j(x,y)$ , with eigenvalues  $\gamma_{983} = 257.1934E_1$ ,  $\gamma_{985} = 257.9339E_1$ ,  $\gamma_{989} = 258.6655E_1$ , and  $\gamma_{990} = 258.9072E_1$ , where  $E_1 = \hbar^2 \pi^2 / 2md^2$ . The Husimi plots in Figs. 2(c) and 2(d) show that these basis states reside on nonlinear resonances of the underlying classical phase space. In Sec. IV, we will show that these basis states give the primary contribution to sharp resonances in the transmission at these cavity parameters.

Inside the lead, we must distinguish between propagating and evanescent modes. The longitudinal component of the eigenstates in the leads, for propagating modes, can be written as

$$\Gamma_n \chi_n(x) = \frac{a_n}{\sqrt{k_n}} e^{-ik_n x} + \frac{b_n}{\sqrt{k_n}} e^{ik_n x}, \quad (2.4)$$

where the wave vector  $k_n$  is given by

$$k_n = \sqrt{\frac{2mE}{\hbar^2} - \left(\frac{n\pi}{d}\right)^2}.$$

If there are  $N$  propagating modes then  $n = 1, \dots, N$ . Here we use a unit current normalization. A particle propagating in the  $n$ th channel has energy in the interval  $n^2 E_1 \leq E \leq (n+1)^2 E_1$ , where  $E_1 = \hbar^2 \pi^2 / 2md^2 = 0.0738 \text{ eV}$ . All remaining modes,  $n = N+1, \dots, \infty$ , are evanescent and can be represented in terms of the states,

$$\Gamma_n \chi_n(x) = \frac{c_n}{\sqrt{\kappa_n}} e^{-\kappa_n |x|}, \quad (2.5)$$

where

$$\kappa_n = \sqrt{\left(\frac{n\pi}{d}\right)^2 - \frac{2mE}{\hbar^2}}.$$

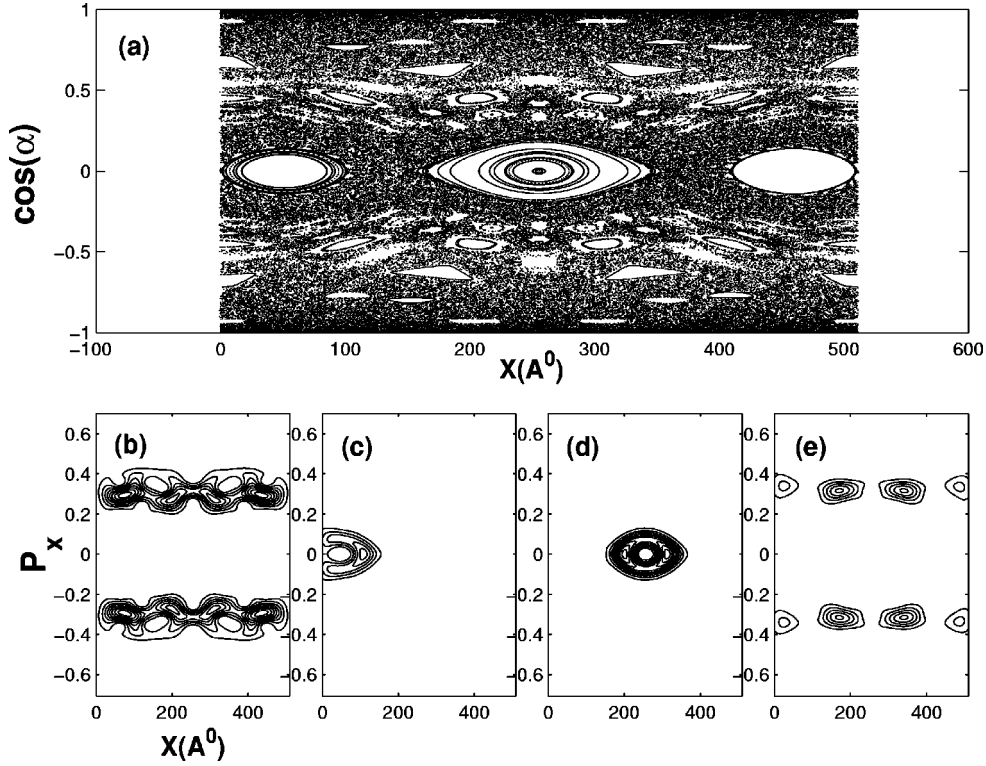


FIG. 2. Surfaces of section for  $L = 511 \text{ \AA}$ ,  $d = 101 \text{ \AA}$ , and  $a = 1 \text{ \AA}$ . (a) A Poincaré surface of section showing  $p_x/p = \cos(\alpha)$  vs  $x$ , each time the particle hits the bottom wall. (b) Husimi plot of quantum surface of section (QSS) for cavity eigenstate with  $\lambda_j = 257.1934E_1$ . (c) QSS for cavity eigenstate with  $\lambda_j = 257.9339E_1$ . (d) QSS for cavity eigenstate with  $\lambda_j = 258.6655E_1$ . (e) QSS for cavity eigenstate with  $\lambda_j = 258.9072E_1$ .

In Ref. [20], we showed that the evanescent modes for this system do not make a significant contribution to the scattering properties that we are interested in. Therefore we will neglect the evanescent modes in subsequent sections.

As shown in Ref. [20], the eigenvalue equation  $\hat{H}|E\rangle = E|E\rangle$  leads to the relation

$$\gamma_j = \frac{\hbar^2}{2m} \frac{1}{(E - \lambda_j)} \sum_{n=1}^N \phi_{j,n}^*(0) \left( \frac{d\chi_n}{dx} \right)_{x=0} \Gamma_n. \quad (2.6)$$

Also, continuity of energy eigenstates at  $x=0$  gives

$$\Gamma_n \chi_n(0) = \sum_{j=1}^M \gamma_j \phi_{j,n}(0) = \sum_{n'=1}^N R_{n,n'} \left( \frac{d\chi_n}{dx} \right)_{x=0} \Gamma_{n'}, \quad (2.7)$$

where

$$R_{n,n'} = \frac{\hbar^2}{2m} \sum_{j=1}^M \frac{\phi_{j,n'}^*(0) \phi_{j,n}(0)}{(E - \lambda_j)} \quad (2.8)$$

is the  $(n, n')$ th matrix element of the reaction matrix [18]. The quantity  $\phi_{j,n}(0)$  is a measure of the overlap between the  $j$ th cavity state, and the  $n$ th channel in the lead, evaluated at the interface,

$$\phi_{j,n}(0) = \sqrt{\frac{2}{d}} \int_0^d dy \phi_j(0, y) \sin\left(\frac{n\pi y}{d}\right). \quad (2.9)$$

Let us now form an  $N \times 1$  column matrix  $\bar{b}$  ( $\bar{a}$ ) whose matrix elements consist of the  $N$  probability amplitudes  $\{b_n\}$  ( $\{a_n\}$ ) of the outgoing (incoming) *propagating* modes. The waveguide scattering matrix ( $S$  matrix)  $\bar{S}$  is an  $N \times N$  matrix which connects the incoming propagating modes to the outgoing propagating modes,  $\bar{b} = \bar{S}\bar{a}$ .

For the case when there are  $N$  propagating modes in the lead we can obtain an  $N \times N$   $S$  matrix that may be written as

$$\bar{S} = - \frac{(\bar{I}_N - i\bar{K})}{(\bar{I}_N + i\bar{K})}, \quad (2.10)$$

where  $\bar{I}_N$  is  $N \times N$  unit matrix, and the  $N \times N$  matrix  $\bar{K}$  has matrix elements  $\bar{K}_{n,n'} = \sqrt{k_n} R_{n,n'} \sqrt{k_{n'}}$  and can be written as

$$\bar{K} = \bar{w}^\dagger \frac{1}{E\bar{I}_M - \bar{H}_{in}} \bar{w}. \quad (2.11)$$

In Eq. (2.11),  $\bar{I}_M$  is the  $M \times M$  unit matrix,  $\bar{H}_{in}$  is an  $M \times M$  diagonal matrix formed with the eigenvalues  $\lambda_j$  ( $j = 1, \dots, M$ ) in the cavity, and  $\bar{w}$  is an  $M \times N$  coupling matrix,

$$\bar{w} = \begin{pmatrix} w_{1,1} & \cdots & w_{1,N} \\ \vdots & & \vdots \\ w_{M,1} & \cdots & w_{M,N} \end{pmatrix}, \quad (2.12)$$

where  $w_{j,n'} = \phi_{j,n'}(0)\sqrt{k_n}$ . With some algebra, the  $S$  matrix can also be written in the form

$$\bar{S} = - \left( \bar{I}_N - 2i\bar{w}^\dagger \frac{1}{E\bar{I}_M - \bar{H}_{in} + i\bar{w}\bar{w}^\dagger} \bar{w} \right). \quad (2.13)$$

In Ref. [20], we showed that if evanescent modes are included, an additional term appears in the denominator in Eq. (2.13).

The reaction matrix approach to waveguide scattering provides a very efficient means of computing the statistical properties of the scattering process because the Schrödinger equation only needs to be solved once to obtain the basis states and eigenvalues in the cavity. Using these values, the  $S$  matrix can then be obtained at all other particle energies  $E$ . Typically for the ripple cavity in Fig. 1, we can obtain the scattering matrix at  $10^5$  different values of incident energy in a reasonable amount of time on a Cray machine.

One of the goals of this paper is to compare the statistical properties of the deterministic scattering process in the ripple cavity to statistical properties of a hypothetical scattering process in which  $\hat{H}_{in}$  is replaced by a diagonal matrix  $\hat{H}_{goe}$  composed of the  $M$  eigenvalues of an  $M \times M$  Gaussian orthogonal ensemble (GOE) Hamiltonian  $\hat{H}'_{goe}$ , and the  $N$  columns of the coupling matrix  $\bar{w}$  are replaced by  $N$  of the  $M$  normalized eigenvectors of  $\hat{H}'_{goe}$  to yield a coupling matrix  $\hat{w}_{goe}$  [4,29]. In this random matrix theory approach, the strength of the coupling between the cavity and the lead is given by the phenomenological parameter  $g$ . The parameter  $g$  does not appear in the deterministic scattering process. For deterministic scattering, the strength of the coupling is entirely determined by the geometry and the potentials at the interface. The scattering matrix, obtained from the RMT, can then be written as

$$\bar{S}_{goe} = - \left( \bar{I}_N - 2ig\bar{w}_{goe}^\dagger \frac{1}{E\bar{I}_M - \bar{H}_{goe} + ig\bar{w}_{goe}\bar{w}_{goe}^\dagger} \bar{w}_{goe} \right). \quad (2.14)$$

It was shown in Ref. [30], using supersymmetry techniques, that for the case when the distribution of energy eigenvalues of  $\hat{H}_{goe}$  is centered at  $E=0$  and  $M \rightarrow \infty$ , the average  $S$  matrix can be written as

$$\langle \bar{S}_{goe} \rangle = s\bar{I}_N \quad \text{with} \quad s = \frac{1 - g[iE/2 + \pi\nu(E)]}{1 + g[iE/2 + \pi\nu(E)]}, \quad (2.15)$$

where  $\nu(E) = \pi^{-1}\sqrt{1 - (E/2)^2}$  is the average density of energy eigenstates. It is useful to introduce the quantity

$$\mu = \mu_r + i\mu_i = \frac{1-s}{1+s^*} = g\nu\pi + ig\frac{E}{2}, \quad (2.16)$$

where  $\mu_r = g\nu\pi$  and  $\mu_i = g(E/2)$ , respectively, are the real and imaginary parts of  $\mu$ . The case when  $g=1$  corresponds to ideal coupling. In the neighborhood of  $E \approx 0$ , the eigen-

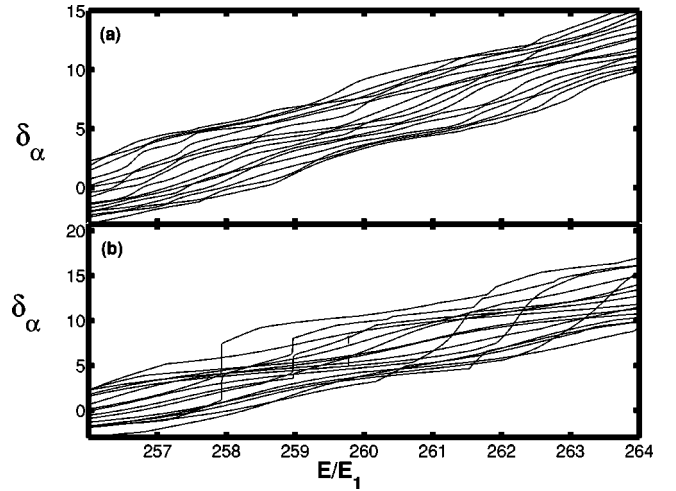


FIG. 3. Eigenphases  $\delta_\alpha$  vs  $E/E_1$  for the energy interval  $256 \leq E/E_1 \leq 272$ : (a)  $a = 25 \text{ \AA}$ , (b)  $a = 1 \text{ \AA}$ .

values of  $\hat{H}_{goe}$  have a constant density,  $1/2\pi$ , and the average  $S$  matrix  $\langle \bar{S}_{goe} \rangle = 0$ . When  $g \neq 1$ , the average  $S$  matrix cannot be zero.

### III. EIGENPHASES OF THE SCATTERING MATRIX

We have analyzed some of the statistical properties of the eigenphases of the  $S$  matrix for the case of deterministic scattering from the ripple cavity for the cases when the internal dynamics in the cavity is completely chaotic and when it is near integrable. In this section, we consider the energy interval  $256E_1 \leq E \leq 289E_1$  when 16 channels are present in the lead. The  $S$  matrix is a  $16 \times 16$  matrix, and for each value of incident energy it has 16 eigenvalues,  $e^{i\delta_\alpha}$  ( $\alpha = 1, \dots, 16$ ), and 16 eigenfunctions,  $|\delta_\alpha\rangle$  ( $\langle \bar{S} | \delta_\alpha \rangle = e^{i\delta_\alpha} |\delta_\alpha\rangle$ ). The  $S$  matrix is unitary so that the eigenfunctions  $|\delta_\alpha\rangle$  form a complete orthonormal set. We can use the orthonormality of the eigenfunctions to follow each eigenphase,  $\delta_\alpha$ , continuously as a function of energy [31]. The eigenfunctions, for two  $S$  matrices evaluated at nearby energies, will be approximately orthogonal if they do not belong to the same eigenphase. Thus we can plot each of the 16 different eigenphases as a function of the incident energy. These are shown in Fig. 3 where the eigenphases, which are defined as mod  $2\pi$ , are “unwrapped” and allowed to evolve continuously as a function of energy. In Fig. 3(a), we show the case with ripple amplitude,  $a = 25 \text{ \AA}$ , where the classical cavity dynamics is chaotic, and in Fig. 3(b) we show the case  $a = 1 \text{ \AA}$  where the classical cavity dynamics is mixed (see Fig. 2). The case of mixed dynamics shows many more abrupt changes of phase as a function of energy than the chaotic case. This is due to the fact that the mixed dynamics has many long lived resonances not found in the chaotic case. This was also seen in Refs. [31,27]. We shall return to this feature in Sec. IV.

Below we first discuss the effect of direct processes on the distribution of eigenphases, and then we determine the distribution of nearest neighbor spacings of these eigenphases.

### A. Distribution of eigenphases

When a scattering process has a nonzero average  $S$  matrix  $\langle \bar{S} \rangle$ , it indicates that direct processes may play a significant role in the scattering process. Direct processes are generally scattering events which do not interact significantly with the reaction region (cavity) [32]. When direct processes are present, the distribution of  $S$ -matrix elements that minimizes information about the scattering process is the Poisson kernel. For the case of an  $N$ -channel process whose dynamics is time reversal invariant, the Poisson kernel has the form

$$P_N(\bar{S}) = \frac{1}{\Omega} \frac{[\text{Det}(1 - \langle S \rangle^* \langle S \rangle)]^{(N+1)/2}}{|\text{Det}(1 - \langle S \rangle^* \bar{S})|^{(N+1)}}, \quad (3.1)$$

where  $\Omega$  is a normalization factor that ensures that the Poisson kernel satisfies the normalization condition,  $\int d\bar{S} P_N(\bar{S}) = 1$ .

The  $S$  matrix can be diagonalized by a unitary matrix  $\bar{U}$  and, as mentioned earlier, the eigenvalues of the  $S$  matrix are denoted by  $e^{i\delta_\alpha}$ ,  $\alpha = 1, \dots, N$ . In terms of the eigenphases  $\delta_\alpha$ , the normalization condition for the Poisson kernel, Eq. (3.1), can be written as

$$\begin{aligned} \int d\bar{S} P_N(\bar{S}) &= \int \cdots \int d\delta_1 \cdots d\delta_N P_N(\delta_1, \dots, \delta_N) \\ &= \frac{1}{\Omega_U} \int \cdots \int d\delta_1 \cdots d\delta_N \\ &\quad \times \prod_{1 \leq \alpha < \alpha' \leq N} |e^{i\delta_\alpha} - e^{i\delta_{\alpha'}}| \\ &\quad \times \left( \frac{(1 - s^* s)^N}{\prod_{\alpha=1}^N (1 - s^* e^{i\delta_\alpha})(1 - s e^{-i\delta_\alpha})} \right)^{(N+1)/2} \\ &= 1, \end{aligned} \quad (3.2)$$

where  $\Omega_U$  is a normalization constant. Note that  $P_N(\delta_1, \dots, \delta_N)$  is the joint probability density to find the angles,  $\delta_\alpha$ , in the intervals  $\delta_\alpha \rightarrow \delta_\alpha + d\delta_\alpha$  ( $\alpha = 1, \dots, N$ ).

In Ref. [33], it is shown that if the following change of angles is introduced,

$$\tan\left(\frac{\theta_\alpha}{2}\right) = \frac{1}{g\pi\nu} \left[ \tan\left(\frac{\delta_\alpha}{2}\right) + g \frac{E}{2} \right], \quad (3.3)$$

and if one assumes ideal coupling  $g=1$ , then Eq. (3.2) reduces to

$$\begin{aligned} \int d\bar{S} P_N(\bar{S}) &= \int \cdots \int d\theta_1 \cdots d\theta_N P_N(\theta_1, \dots, \theta_N) \\ &= \frac{1}{\Omega_U} \int \cdots \int d\theta_1 \cdots d\theta_N \\ &\quad \times \prod_{1 \leq \alpha < \alpha' \leq N} |e^{i\theta_\alpha} - e^{i\theta_{\alpha'}}|, \end{aligned} \quad (3.4)$$

which is just the distribution for the circular orthogonal ensemble (COE) [5,6]. Thus, even for scattering processes which include direct processes, it is possible in principle to transform away the direct processes and compare the eigenphase distribution with that of the COE (note that similar ideas first appeared in literature in Ref. [15]). It is important to note that the transformation that removes direct processes is not the same as the unfolding process that occurs on the energy spectrum of bounded systems to give a constant average density.

In our subsequent analysis, the case of scattering with only a single channel will be useful for analyzing data. For the single-channel scattering ( $N=1$ ), the  $S$  matrix reduces to the complex function  $S = e^{i\delta}$  and the Poisson kernel reduces to [15]

$$P_{1s}(\delta) = \frac{1}{2\pi} \frac{[(1 - s^* s)]}{|(1 - s^* e^{i\delta})|^2}, \quad (3.5)$$

with normalization condition  $\int_{-\pi}^{\pi} d\delta P_{1s}(\delta) = 1$ . Under the transformation above,  $P_{1s}(\delta) \rightarrow P_1(\theta) = 1/2\pi$ , which is the COE prediction.

Having obtained numerical values of the eigenvalues  $e^{i\delta_\alpha}$  as a function of energy, we can compute an average value for each of the 16 eigenvalues,

$$s_\alpha = \langle e^{i\delta_\alpha} \rangle = \frac{1}{\eta} \sum_{k=1}^{\eta} e^{i\delta_\alpha(E_k)}, \quad (3.6)$$

where  $\eta$  is the number of energy values used. The apparently continuous eigenphase curves actually consist of about 40 000 discrete energy points. The approximate orthonormality of  $S$  matrix eigenvectors for neighboring energies has been used to sort the eigenphases. Thus, the eigenphases and eigenvectors have an energy interval over which they are correlated, and we have used that fact in our sorting process. On the other hand, this correlation of the  $S$  matrices at neighboring energies can prevent us from obtaining statistics that can be compared to the RMT predictions. Comparison to the RMT requires use of independent data points. Therefore, in order to study the statistical properties of the eigenphases, we must choose values of the eigenphases separated in energy a distance greater than the correlation length. For each eigenphase curve we select points that have an energy spacing  $\Delta E = 0.495E_1$ . We choose this spacing based on an analysis of the delay time correlation discussed in Sec. IV. (The delay time autocorrelation function is the second derivative of the eigenphase autocorrelation function.)

We have computed a histogram of the number of eigenphases  $N(\delta) = \eta P_N(\delta)$  versus value of eigenphase  $\delta_\alpha$  in the 16-channel region, where  $\eta$  is the number of data points. In order to improve the statistics, we use data from four different ripple amplitudes,  $a = 25 \text{ \AA}$ ,  $30 \text{ \AA}$ ,  $35 \text{ \AA}$ ,  $45 \text{ \AA}$ , all of which lie in the chaotic regime. All eigenphases lie in the energy interval  $256 < E/E_1 < 289$  and have energy spacing  $\Delta E = 0.495E_1$ . Thus the histogram includes  $67 \times 16 \times 4 = 4288$  data points. We have found that the distribution of eigenphases, along a given eigenphase curve, is well described by the Poisson kernel for the single-channel case. We

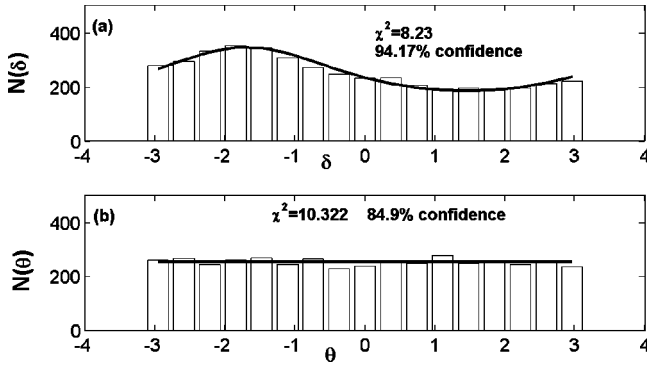


FIG. 4. (a) Histogram of number of eigenphases  $N(\delta)$  vs  $\delta$  for the 16-channel energy interval  $256 \leq E/E_1 \leq 289$ , and for four different ripple sizes,  $a = 25 \text{ \AA}$ ,  $30 \text{ \AA}$ ,  $35 \text{ \AA}$ ,  $45 \text{ \AA}$ . The solid line is a plot of the single-channel Poisson kernel with  $\langle S \rangle = \sum_{\alpha=1}^{64} \langle e^{i\delta_\alpha} \rangle$  and normalized to the number of eigenphases. (b) Histogram of transformed eigenphases  $\theta_\alpha$  for all 64 eigenphase curves. For all cases,  $d = 101 \text{ \AA}$  and  $L = 511 \text{ \AA}$ . A  $\chi^2$  test result is also shown for both plots with 17 bins taken into account.

proceed as follows. We compute the average eigenvalue,  $s_\alpha = \langle e^{i\delta_\alpha} \rangle$ , for each eigenphase curve. We can form a histogram using the 67 data points from a single eigenphase curve. We do this for each of the 64 eigenphase curves, using the same number of bins and bin width for each curve. We then add these 64 histograms together to form a single histogram, which is shown in Fig. 4(a). The solid line in Fig. 4(a) is the single-channel Poisson kernel  $P_1(\delta)$ , but with  $\langle s \rangle = (1/64) \sum_{\alpha=1}^{64} s_\alpha$ . We can use Eq. (3.3) to transform away the effects of the direct interactions and find the distribution of the transformed angles,  $\theta_\alpha$ . If we use Eq. (2.16) and obtain  $\mu$  from the numerically calculated values of  $s_\alpha = \langle e^{i\delta_\alpha} \rangle$ , then the transformed angles  $\theta_\alpha$  are given by

$$\tan\left(\frac{\theta_\alpha}{2}\right) = \frac{1}{\mu_r} \left[ \tan\left(\frac{\delta_\alpha}{2}\right) + \mu_i \right], \quad (3.7)$$

with  $\mu_r$  and  $\mu_i$  computed numerically from  $s_\alpha$ . In Fig. 4(b), we show how the histogram in Fig. 4(a) changes if we transform each eigenphase  $\delta_\alpha$  using Eq. (3.7). In this case distribution is approximately constant and equal to the area,  $N/2\pi$ . Thus, having transformed away the contribution from the direct processes, we obtain the COE eigenphase distribution for this chaotic scattering process, with fairly high confidence level.

For  $a = 1 \text{ \AA}$  the plots of the eigenphase distributions look very similar to the chaotic case shown in Fig. 4, and it appears that the eigenphase distribution is not as sensitive an indicator for underlying chaos as is the nearest neighbor spacing distribution, at least with this type of analysis.

### B. Nearest neighbor eigenphase spacing

In this section, we consider the nearest neighbor spacings between eigenphases  $\delta_\alpha$  of the scattering matrix for the 16-channel case in the energy interval  $256 < E/E_1 < 289$ . For any given value of the energy, the  $S$  matrix only has 16 eigenphases. However, we can form a histogram of nearest

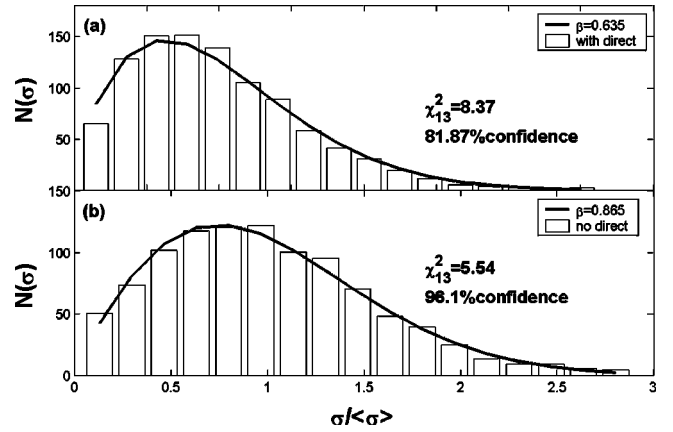


FIG. 5. Histogram of number,  $N(\sigma)$ , of nearest neighbor scaled eigenphase spacings,  $\sigma$ , for the chaotic regime with  $d = 101 \text{ \AA}$ ,  $L = 511 \text{ \AA}$ . The average spacing  $\langle \sigma \rangle$  is obtained for each eigenphase curve. The histograms contain a total of  $15 \times 67 = 1005$  data points averaged over four different ripple sizes,  $a = 25 \text{ \AA}$ ,  $30 \text{ \AA}$ ,  $35 \text{ \AA}$ ,  $45 \text{ \AA}$ . (We obtain a histogram for each of the four values of the ripple amplitude. We then add them and divide by four.) (a) Before direct processes are transformed away. The thin solid line is the Brody distribution with  $\beta = 0.635$ . (b) After direct processes transformed away. The thin solid line is the Brody distribution with  $\beta = 0.865$ . A  $\chi^2$  test result is also shown for both plots with 13 bins in it taken into account

neighbor eigenphase spacings if we obtain eigenphase spacings for a sequence of different energies in the range  $256 < E/E_1 < 289$ . In Fig. 5(a) we show histograms of 1005 ( $15 \times 67$ ) nearest neighbor spacings for eigenphases computed at energy increments  $\Delta E = 0.495E_1$  and obtained by averaging over histograms for each ripple amplitude,  $a = 25 \text{ \AA}$ ,  $30 \text{ \AA}$ ,  $35 \text{ \AA}$ ,  $45 \text{ \AA}$ . We have fit the histogram to the Brody distribution [29]

$$P_B(\sigma) = A \left( \frac{\sigma}{\langle \sigma \rangle} \right)^\beta \exp \left[ -\xi \left( \frac{\sigma}{\langle \sigma \rangle} \right)^{1+\beta} \right]$$

with

$$\xi = \left[ \frac{1}{\langle \sigma \rangle} \Gamma \left( \frac{2+\beta}{1+\beta} \right) \right]^{1+\beta}, \quad (3.8)$$

$\langle \sigma \rangle$  is the average spacing between nearest neighbor eigenphases, and  $\Gamma(x)$  is the gamma function. In Fig. 5(a), the solid line is a fit to the Brody distribution for  $\beta = 0.635$ . In Fig. 5(b), same calculation is performed after direct processes were transformed away. In this case  $\beta = 0.865$ . Note that the GOE prediction ( $\beta = 0.95$ ) for the closed system eigenvalue spacings is fairly close to our value of  $\beta$ , after the effects of direct processes are transformed away. In Ref. [28], the nearest neighbor energy eigenvalue spacings for a closed ripple billiard were fit to the Brody distribution with  $\beta = 0.806$ . In that case, the deviation from the GOE predictions was found to be due to bouncing ball orbits. Our result also contains bouncing ball contributions. It is useful to note that in our scattering system there is no long range energy correlation for the 16-channel region (we have explicitly re-

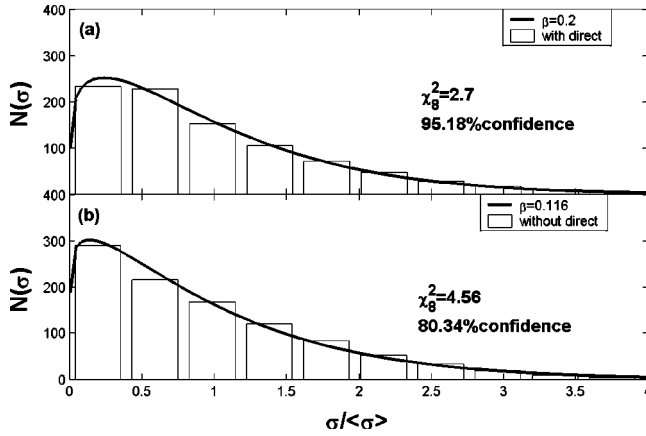


FIG. 6. Histogram of number,  $N(\sigma)$ , of nearest neighbor eigenphase spacings,  $\sigma$ , for the near-integrable regime with  $d=101 \text{ \AA}$ ,  $L=511 \text{ \AA}$ . The histograms contain a total of 1005 data points averaged over six different ripple sizes,  $a=0.5 \text{ \AA}$ ,  $1 \text{ \AA}$ ,  $2 \text{ \AA}$ ,  $3 \text{ \AA}$ ,  $4 \text{ \AA}$ ,  $5 \text{ \AA}$ . (a) Before direct processes are transformed away. The thin solid line is the Brody distribution with  $\beta=0.2$ . (b) After direct processes are transformed away. The thin solid line is the Brody distribution with  $\beta=0.116$ . A  $\chi^2$  test result is also shown for both plots with 8 bins taken into account

moved energy correlations by taking data points at large energy increments), in contrast to the case reported in Ref. [34]

We also obtained a nearest neighbor spacing histogram for the case with mixed phase space in the 16-channel energy interval. In Fig. 6(a), we show the histogram of nearest neighbor eigenphase spacings for  $a=0.5 \text{ \AA}$ ,  $1 \text{ \AA}$ ,  $2 \text{ \AA}$ ,  $3 \text{ \AA}$ ,  $4 \text{ \AA}$ ,  $5 \text{ \AA}$  in the energy interval  $256 < E/E_1 < 289$  before direct processes are transformed away. We use an energy spacing  $\Delta E = 0.495 E_1$  and obtain 1005 data points for each amplitude. We then average over the histograms for the six ripple amplitudes. The solid line is a fit to the Brody distribution for  $\beta=0.2$ . In Fig. 6(b), the same histogram is shown after direct processes are transformed away. The Brody parameter in this case is  $\beta=0.116$ , which is closer to a Poisson distribution (the Brody distribution becomes a Poisson distribution for  $\beta=0$ ).

The distribution of nearest neighbor eigenphase spacings has been computed for a energy independent scattering matrix in Ref. [35] for a very different physical system. They also report close agreement with the COE predictions for the chaotic region, although they do not have to deal with direct processes. It is clear that direct processes can play an important role in causing deviations from random matrix theory predictions for scattering processes.

#### IV. PARTIAL DELAY TIMES

In this section we compare the partial delay time distribution, computed for the deterministic scattering process, to values obtained from the random matrix theory. The partial delay times are given by the energy derivative of eigenphases,  $\tau_\alpha = \hbar(d\delta_\alpha/dE)$  [36]. The average partial delay time density for a scattering process governed by the scattering matrix,  $\bar{S}_{goe}$ , has been computed in Refs. [37,33], using su-

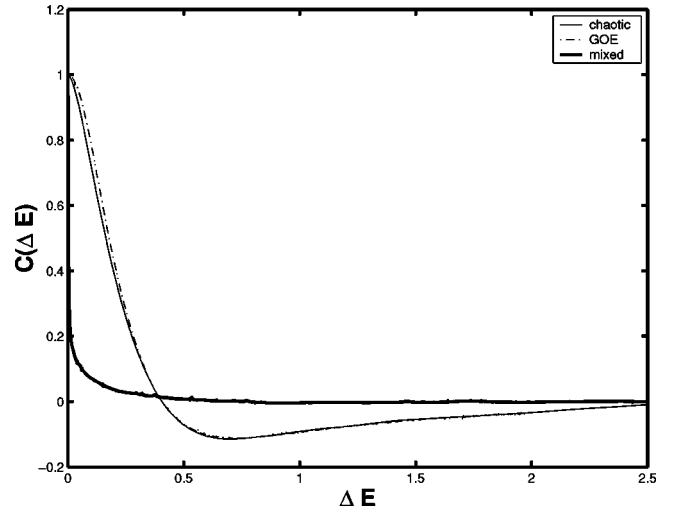


FIG. 7. The autocorrelation function of time delays in the 16-channel energy interval  $256 < E/E_1 < 289$ . The thin line is obtained numerically for the chaotic regime, using six different ripple amplitudes,  $a=22 \text{ \AA}$ ,  $23 \text{ \AA}$ ,  $24 \text{ \AA}$ ,  $25 \text{ \AA}$ ,  $26 \text{ \AA}$ ,  $27 \text{ \AA}$ , with direct processes transformed out of the data. An autocorrelation function is obtained for each partial time delay curve and the average of those 96 autocorrelation functions is shown. The dotted-dashed line is the GOE result for perfect coupling with 16 modes with the average density of states chosen equal to 1.25. The thick line represents the numerically obtained autocorrelation function in the region of mixed phase space for  $a=0.5 \text{ \AA}$ ,  $1 \text{ \AA}$ ,  $2 \text{ \AA}$ ,  $3 \text{ \AA}$ ,  $5 \text{ \AA}$ .

persymmetry techniques, and is given by

$$\rho(\tau) = (1/N) \sum_{\alpha} \langle \delta(\tau - \tau_{\alpha}) \rangle_{goe} = \frac{(1/2)^{N/2} \exp[-1/2(\tau/\langle\tau\rangle)]}{\Gamma(N/2) (\tau/\langle\tau\rangle)^{N/2+2}}, \quad (4.1)$$

where  $\langle\tau\rangle = 1/N$ .

Before showing the distribution obtained for the partial delay times, it is useful to discuss energy correlations contained in the partial delay time curves. In Fig. 7, we show the autocorrelation function for the partial delay times obtained in the 16-channel energy regime  $256 < E/E_1 < 289$  and averaged over six different ripple sizes,  $a=22 \text{ \AA}$ ,  $23 \text{ \AA}$ ,  $24 \text{ \AA}$ ,  $25 \text{ \AA}$ ,  $26 \text{ \AA}$ ,  $27 \text{ \AA}$ . For each partial delay time curve we obtain an autocorrelation function, and then we average over all 96 curves. We also show the GOE prediction for the 16-channel case as well as the partial delay time autocorrelation function for the near-integrable regime ( $a=1 \text{ \AA}$ ). The GOE prediction is obtained after performing the triple integration given in Ref. [38]. The energy scale is adjusted to correspond to the relevant scale for our data. We also note that the partial delay time autocorrelation function is the second derivative of the eigenphase autocorrelation function. Therefore the eigenphase autocorrelation function decays more slowly than the partial time delay autocorrelation function.

In Fig. 8(a), we show a histogram of the scaled partial delay times,  $\tau/\langle\tau\rangle$ . We again consider the energy regime with 16 channels and vary the energy in the interval  $256 E_1$

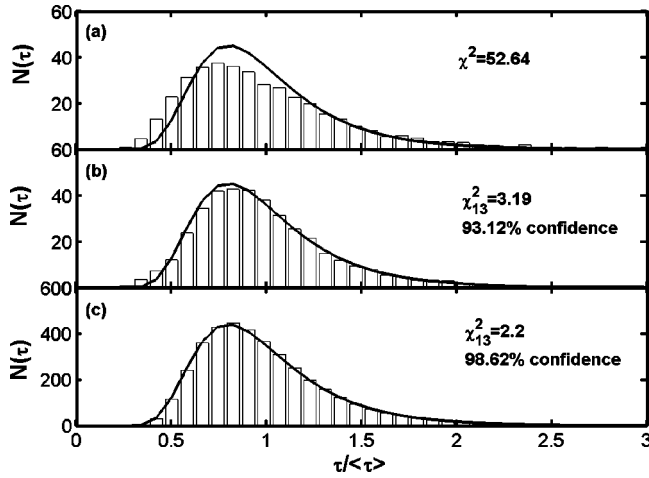


FIG. 8. Histogram of number of scaled partial delay times,  $N(\tau)$ , vs  $\tau/\langle\tau\rangle$ , for the 16-channel energy interval  $256 \leq E/E_1 \leq 289$ , with  $d=101 \text{ \AA}$  and  $L=511 \text{ \AA}$ . Data for ripple amplitudes  $a=25 \text{ \AA}$ ,  $30 \text{ \AA}$ ,  $35 \text{ \AA}$ ,  $45 \text{ \AA}$  is included in the histograms. Data points are taken at energy intervals,  $\Delta E=0.33E_1$ . (a) Histogram of scaled partial delay times taken from eigenphase curves for  $\delta_\alpha$ . A scaling factor  $\langle\tau\rangle$  is obtained for each eigenphase curve. (b) Histogram of scaled partial delay times taken from eigenphase curves for the transformed eigenphases,  $\theta_\alpha$ . (c) Histogram of partial delay times obtained from the  $16 \times 16$   $S$  matrix  $\bar{S}_{goe}$  (includes 4000 data points). A  $\chi^2$  test result is also shown for the plots (b) and (c) with 13 bins taken into account.

$\langle E \rangle < 289E_1$ . To obtain enough values to build good statistics, we use four different ripple sizes,  $a=25 \text{ \AA}$ ,  $30 \text{ \AA}$ ,  $35 \text{ \AA}$ ,  $45 \text{ \AA}$ . For these ripple amplitudes, the ripple cavity dynamics is chaotic. We used 100 energy points per specific ripple size, and therefore an energy increment of  $\Delta E=0.33E_1$ . The average delay time  $\langle\tau\rangle$  is obtained numerically for each partial delay time curve. Then the histograms for 64 scaled partial delay times are combined into one histogram by simply adding values in the corresponding bins. The solid line in Fig. 8(a) is a plot of the RMT prediction,  $N(\tau) = \eta' \rho(\tau)$ , where  $\eta'$  is the area under the curve and  $\langle\tau\rangle = 1/N$ . The agreement is not good because our data contain the effect of direct scattering processes. In Fig. 8(b), we show the partial delay time density obtained from the eigenphases  $\theta_\alpha$ , which no longer contain the effect of direct scattering processes. The solid line is a plot of  $N(\tau)$  with  $\langle\tau\rangle = 1/N$  [37]. The agreement is very good. Finally in Fig. 8(c), we plot histogram of 4000 partial delay times obtained from a  $16 \times 16$   $\bar{S}_{goe}$  by using different realizations. Again, the agreement between the data and Eq. (4.1) is very good. Thus, after the removal of the effects of direct scattering processes our deterministic scattering from the chaotic ripple cavity behaves very much like the RMT prediction. (It is useful to note that in Ref. [20], we compared the Wigner-Smith delay time distribution with numerically computed predictions of the RMT. The Wigner-Smith delay time is defined as  $\tau_{ws} = (1/N) \sum_{\alpha=1}^N \tau_\alpha$ .)

In Fig. 9, we show the delay time distributions for the near-integrable case,  $a=1 \text{ \AA}$ . We have used energy increments  $\Delta E=0.1E_1$  justified from Fig. 7. The delay time dis-

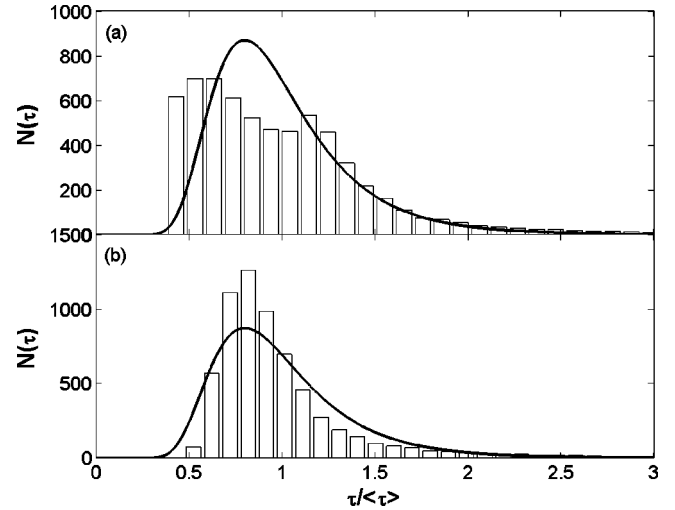


FIG. 9. Histogram of partial delay times for the 16-channel energy interval  $256 \leq E/E_1 \leq 289$ , with  $d=101 \text{ \AA}$  and  $L=511 \text{ \AA}$ . Data for ripple amplitudes,  $a=0.5 \text{ \AA}$ ,  $1 \text{ \AA}$ ,  $2 \text{ \AA}$ ,  $3 \text{ \AA}$ ,  $5 \text{ \AA}$ , is used to construct the histograms. Data points are taken at energy spacings  $\Delta E=0.1E_1$ . A total of  $400 \times 16$  points is used. (a) Histogram of scaled partial delay time curves taken from eigenphase curves for  $\delta_\alpha$ . (b) Histogram of scaled partial delay times taken from curves for transformed eigenphases,  $\theta_\alpha$ .

tribution for the near-integrable case deviates significantly from the random matrix result and the results for chaotic cavity shown in Fig. 8.

Let us now return to the eigenphase curve in Fig. 3(b). We see that the curves for the near-integrable case have a sequence of fairly abrupt large changes of phase. These are due to resonance structures that cause larger than average delays of the particle in the cavity. In Fig. 10, we plot the Wigner-Smith delay time (which is an average over all partial delay times) in the energy interval  $257.4 \leq E/E_1 \leq 259.5$ . This en-

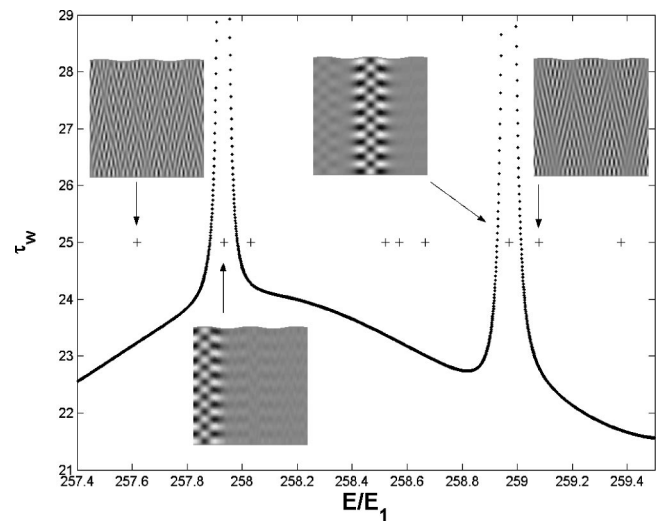


FIG. 10. Plot of Wigner-Smith delay time in the energy interval  $257.4 \leq E/E_1 \leq 259.5$  for  $d=101 \text{ \AA}$ ,  $L=511 \text{ \AA}$ ,  $a=1 \text{ \AA}$ . Crosses show values of cavity basis state energies in this interval. Insets show the spatial distribution of four cavity basis states, two at resonance and two off resonance.

ergy interval contains two of the large phase changes in the eigenphase curves in Fig. 3(b). We see that each large phase change gives rise to a large peak in the delay time. The crosses in Fig. 10 give the energies of the cavity basis states,  $\lambda_j$ , in that energy interval. There appears to be one cavity state which lies at each resonance energy. In Fig. 10, we have also plotted the configuration space distribution of four of the cavity eigenstates, two at resonance and two off resonance. In Figs. 2(b)–2(e), we have shown Husimi plots of the quantum Poincaré surface of section for each of these four states. The two states giving rise to the delay time resonance peaks lie in the dominant nonlinear resonance structures in the classical phase space. The quantum particle appears to tunnel into these dynamical resonance structures, and is delayed there for a considerable length of time.

## V. CONCLUSION

We have analyzed the statistical properties of a scattering process in a waveguide with a cavity that allows a range of dynamics, including integrable, mixed, or chaotic. In this waveguide, direct processes also play an important role. The “ripple” cavity that we use has the special feature that it allows us to form a Hamiltonian matrix to describe the dynamics interior to the cavity. This, in turn, allows us to use the reaction matrix approach to scattering for our deterministic scattering process. The reaction matrix approach is one of the most efficient methods for obtaining the large amounts of data necessary to obtain good statistics. Until now, mesh based models (such as the boundary element method, finite element method, or recursive Green’s function method) were the main numerical methods to deal with scattering problems. However, these methods use an energy dependent boundary condition which makes it a formidable task to obtain solutions for very large numbers of energy points. The reaction matrix approach allows us to circumvent this problem. It is also useful to note that the reaction matrix approach has been used extensively to study properties of the complex

poles of the  $S$  matrix. This is discussed in some detail in Refs. [35,39–41].

We have obtained a number of results. We find that, in the near-integrable regime, nonlinear resonances in the classical phase space give rise to large eigenphase excursions and long delay times for quantum particles that can tunnel into these dynamical structures.

We have focused much of our discussion on the energy regime in which 16 channels are open in the lead. We have been able to follow each eigenphase of the  $S$  matrix continuously as a function of energy. We have examined the statistical properties of the scattering process by gathering data about each eigenphase at discrete energy intervals in the 16-channel regime. This assumes a kind of “stationarity” as a function of energy of the underlying scattering process. We have chosen the energy intervals so that our data points are statistically independent.

We have shown, for the scattering system considered here, that the effect of direct processes on the eigenphase curves can be transformed away. We find that, for the case where the cavity dynamics is classically chaotic, a partial time delay density histogram, formed from all 16 transformed eigenphase curves, agrees to 96% confidence level with a Brody distribution with Brody parameter  $\beta=0.87$ . Similar deviations from the GOE prediction of  $\beta=0.95$  have been seen in the nearest neighbor energy eigenvalue spacing distributions of closed ripple billiards [28] and in that case are caused by bouncing ball orbits. We expect that the same mechanism is having an effect here.

## ACKNOWLEDGMENTS

The authors wish to thank the Welch Foundation (Grant No. F-1051); the NSF (Grant No. INT-9602971); and the U.S. DOE (Contract No. DE-FG03-94ER14405) for partial support of this work. We also thank the University of Texas at Austin High Performance Computing Center for use of their computer facilities.

- 
- [1] E.P. Wigner, *Canadian Mathematical Congress Proceedings* (University of Toronto Press, Toronto, 1957).
  - [2] J. Garg, J. Rainwater, J.S. Petersen, and W.W. Havens, Jr., *Phys. Rev.* **134**, 985 (1964).
  - [3] T.A. Brody, J. Flores, J.B. French, P.A. Mello, A. Pandey, and S.S.M. Wong, *Rev. Mod. Phys.* **53**, 385 (1981).
  - [4] M.L. Mehta, *Random Matrices and the Statistical Theory of Energy Levels*, 2nd ed. (Academic Press, New York, 1991).
  - [5] F.J. Dyson, *J. Math. Phys.* **3**, 140 (1962); **3**, 157 (1962); **3**, 166 (1962); **3**, 344 (1962).
  - [6] L.K. Hua, *Harmonic Analysis of Functions of Several Complex Variables in the Classical Domains* (American Mathematical Society, Providence, 1963).
  - [7] S.W. MacDonald and A.N. Kaufman, *Phys. Rev. Lett.* **42**, 1189 (1979).
  - [8] O. Bohigas, M.J. Giannoni, and C. Schmit, *Phys. Rev. Lett.* **52**, 1 (1984).
  - [9] G. Casati, F. Valz-Gris, and I. Guarneri, *Lett. Nuovo Cimento Soc. Ital. Fis.* **28**, 279 (1980).
  - [10] M.V. Berry and M. Tabor, *Proc. R. Soc. London, Ser. A* **356**, 375 (1977).
  - [11] L.E. Reichl, *The Transition to Chaos in Classical Conservative Systems: Quantum Manifestations* (Springer-Verlag, New York, 1992).
  - [12] T. Guhr, A. Muller-Groeling, and H.A. Weidenmuller, *Phys. Rep.* **299**, 189 (1998).
  - [13] C. Jung and T.H. Seligman, *J. Phys. A* **28**, 1507 (1995).
  - [14] C. Mahaux and H.A. Weidenmuller, *Shell Model Approach to Nuclear Reactions* (North-Holland, Amsterdam, 1969).
  - [15] G. Lopez, P.A. Mello, and T.H. Seligman, *Z. Phys. A* **302**, 351 (1981).
  - [16] P.A. Mello, P. Pereyra, and T.H. Seligman, *Ann. of Phys.* **161**, 254 (1985); W.A. Friedman and P.A. Mello, *ibid.* **161**, 276 (1985).

- [17] P.W. Brouwer, Phys. Rev. B **51**, 16 878 (1995).
- [18] E.P. Wigner and L.E. Eisenbud, Phys. Rev. E **72**, 29 (1949).
- [19] G.A. Luna-Acosta, Kyungsan Na, L.E. Reichl, and A. Krokhin, Phys. Rev. E **53**, 3271 (1996).
- [20] Gursoy B. Akguc and L.E. Reichl, Phys. Rev. E **64**, 056221 (2001).
- [21] C.M. Marcus, A.J. Rimberg, R.M. Westervelt, P.F. Hopkins, and A.C. Gossard, Phys. Rev. Lett. **69**, 506 (1992).
- [22] A.M. Chang, H.U. Baranger, L.N. Pfeiffer, and K.W. West, Phys. Rev. Lett. **73**, 2111 (1994).
- [23] J.P. Bird, J. Phys.: Condens. Matter **11**, R413 (1999).
- [24] H.-D. Graf, H.L. Harney, H. Lengeler, C.H. Lewenkopf, C. Rangacharyulu, A. Richter, P. Schardt, and H.A. Weidenmuller, Phys. Rev. Lett. **69**, 1296 (1992).
- [25] J. Stein and H.-J. Stöckmann, Phys. Rev. Lett. **68**, 2867 (1992).
- [26] H.-J. Stöckmann, *Quantum Chaos-An Introduction* (Cambridge University Press, Cambridge, 1999).
- [27] G.A. Luna-Acosta, J.A. Mendez-Bermudez, P. Seba, and K.N. Pichugin, Phys. Rev. E **65**, 046605 (2002).
- [28] Wenjun Li, L.E. Reichl, and Biao Wu, Phys. Rev. E **65**, 056220 (2002).
- [29] T.A. Brody, Lett. Nuovo Cimento Soc. Ital. Fis. **7**, 482 (1973).
- [30] J.J.M. Verbaarschot, H.A. Weidenmuller, and M.R. Zirnbauer, Phys. Rep. **129**, 367 (1985).
- [31] Gursoy B. Akguc and L.E. Reichl, J. Stat. Phys. **98**, 813 (2000).
- [32] P.A. Mello and H.U. Baranger, Waves Random Media **9**, 105 (1999).
- [33] Dmitry V. Savin, Yan V. Fyodorov, and H.-J. Sommers, Phys. Rev. E **63**, 035202(R) (2001).
- [34] B. Dietz, M. Lombardi, and T.H. Seligman, J. Phys. A **29**, L95 (1996).
- [35] C. Jung, M. Muller, and I. Rotter, Phys. Rev. E **60**, 114 (1999).
- [36] E.P. Wigner, Phys. Rev. **98**, 145 (1955); F.T. Smith, *ibid.* **118**, 349 (1960); D. Bohm, *Quantum Theory* (Prentice-Hall, Englewood Cliffs, NJ, 1950), p. 260.
- [37] Y.V. Fyodorov and H.-J. Sommers, J. Math. Phys. **38**, 1918 (1997).
- [38] N. Lehman, D.V. Savin, V.V. Sokolov, and H.-J. Sommers, Physica D **86**, 572 (1995).
- [39] I. Rotter, E. Persson, K. Pichugin, and P. Seba, Phys. Rev. E **62**, 450 (2000).
- [40] I. Rotter, Phys. Rev. E **64**, 036213 (2001).
- [41] H.-J. Stockmann, E. Persson, Y.-H. Kim, M. Barth, U. Kuhl, and I. Rotter, Phys. Rev. E **65**, 066211 (2002).